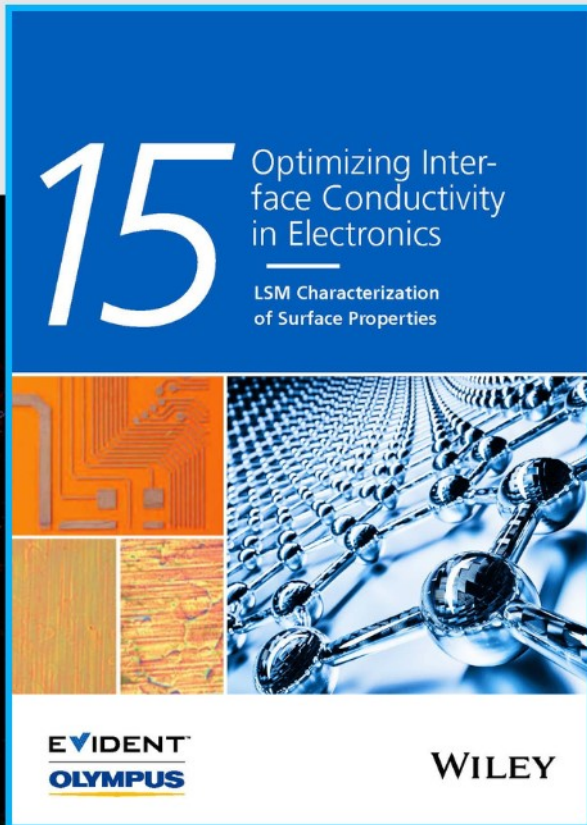




# Optimizing Interface Conductivity in Electronics



The latest eBook from  
**Advanced Optical Metrology.**  
Download for free.

Surface roughness is a key parameter for judging the performance of a given material's surface quality for its electronic application. A powerful tool to measure surface roughness is 3D laser scanning confocal microscopy (LSM), which will allow you to assess roughness and compare production and finishing methods, and improve these methods based on mathematical models.

Focus on creating high-conductivity electronic devices with minimal power loss using laser scanning microscopy is an effective tool to discern a variety of roughness parameters.

**EVIDENT**  
**OLYMPUS**

**WILEY**

# Inkjet-Printed Tungsten Oxide Memristor Displaying Non-Volatile Memory and Neuromorphic Properties

Hongrong Hu, Alexander Scholz, Christian Dolle, Alexander Zintler, Aina Quintilla, Yan Liu, Yushu Tang, Ben Breitung, Gabriel Cadilha Marques, Yolita M. Eggeler, and Jasmin Aghassi-Hagmann\*


Printed electronics including large-area sensing, wearables, and bioelectronic systems are often limited to simple circuits and hence it remains a major challenge to efficiently store data and perform computational tasks. Memristors can be considered as ideal candidates for both purposes. Herein, an inkjet-printed memristor is demonstrated, which can serve as a digital information storage device, or as an artificial synapse for neuromorphic circuits. This is achieved by suitable manipulation of the ion species in the active layer of the device. For digital-type memristor operation resistive switching is dominated by cation movement after an initial electroforming step. It allows the device to be utilized as non-volatile digital memristor, which offers high endurance over 12 672 switching cycles and high uniformity at low operating voltages. To use the device as an electroforming-free, interface-based, analog-type memristor, anion migration is exploited which leads to volatile resistive switching. An important figure of merits such as short-term plasticity with close to biological synapse timescales is demonstrated, for facilitation (10–177 ms), augmentation (10s), and potentiation (35 s). Furthermore, the device is thoroughly studied regarding its metaplasticity for memory formation. Last but not least, the inkjet-printed artificial synapse shows non-linear signal integration and low-frequency filtering capabilities, which renders it a good candidate for neuromorphic computing architectures, such as reservoir computing.

## 1. Introduction

Novel applications, such as soft robotics, wearables, bioelectronics, and smart devices for the Internet of Things (IoT) require flexible, customizable, as well as efficient data storage and computation abilities. Ideally, this can be realized by printed electronics (PE) and printable materials, that offer fabrication on non-conformal surfaces and direct integration into smart objects.<sup>[1,2]</sup> However, currently the performance of printed active devices is still limited.<sup>[3]</sup> Performance limitations and fabrication challenges on device level stem from complex material stacks and interface properties of transistors, requiring either thin dielectric layers or chemically stable polymer electrolytes/ion gels as well as high mobilities of printed semiconductors, to name but a few. This makes realization of printed complex circuitry challenging. In addition, the demand to handle large amounts of data generated in applications such as near-sensor computing,<sup>[4,5]</sup> calls for more efficient information processing beyond

H. Hu, A. Scholz, Y. Liu, Y. Tang, B. Breitung, G. C. Marques, J. Aghassi-Hagmann  
Institute of Nanotechnology (INT)  
Karlsruhe Institute of Technology (KIT)  
76344 Eggenstein-Leopoldshafen, Germany  
E-mail: jasmin.aghassi@kit.edu  
C. Dolle, A. Zintler, Y. M. Eggeler  
Laboratory for Electron Microscopy (LEM)  
Microscopy of Nanoscale Structures and Mechanisms (MNM)  
Karlsruhe Institute of Technology (KIT)  
76131 Karlsruhe, Germany

A. Quintilla  
Nanostructure Service Laboratory (NSL)  
Karlsruhe Institute of Technology (KIT)  
76131 Karlsruhe, Germany  
Y. Tang  
Karlsruhe Nano Micro Facility (KNMF)  
Karlsruhe Institute of Technology (KIT)  
76344 Eggenstein-Leopoldshafen, Germany

 The ORCID identification number(s) for the author(s) of this article can be found under <https://doi.org/10.1002/adfm.202302290>

© 2023 The Authors. Advanced Functional Materials published by Wiley-VCH GmbH. This is an open access article under the terms of the Creative Commons Attribution-NonCommercial License, which permits use, distribution and reproduction in any medium, provided the original work is properly cited and is not used for commercial purposes.

DOI: 10.1002/adfm.202302290

classical von-Neumann computing architectures. In this regard, neuromorphic computing, which attempts to mimic the way a human brain processes information, performs computational tasks efficiently in parallel and is regarded as one of the emerging techniques to tackle data-intensive tasks.<sup>[6–8]</sup>

To facilitate the development of printed neuromorphic circuits, novel electronic devices, such as printable memristors, are required. Compared to transistors, memristors are less complex and provide memory and logic functions in addition to their interesting analog properties suitable for neuromorphic computing.<sup>[6,9–12]</sup> A memristor is a two-terminal electronic device that can be stimulated by an external voltage and change its resistive state accordingly. Multiple materials and material compositions, such as polymers, carbon nanotubes, and metal oxides can be utilized as the active layer in memristors.<sup>[13–15]</sup> Depending on the resistive switching mechanism, memristors can be categorized according to their electrical behavior. This includes analog-type memristors to emulate biological synapses and neurons<sup>[16,17]</sup> and digital-type memristors for data storage applications.<sup>[18]</sup> Most of these devices are fabricated using advanced manufacturing methods, such as atomic layer deposition and magnetron sputtering,<sup>[16–19]</sup> but recently also printing of memristors is becoming more and more popular.<sup>[20–29]</sup>

Regarding printed electronics, digital printing technologies, such as electrohydrodynamic jet-, aerosol-, and inkjet-printing, are of particular interest due to their additive, material efficient, non-contact, and maskless fabrication capabilities.<sup>[30,31]</sup> Recent works on printed memristors mostly focus on digital-type memristors with filamentary type of resistive switching suitable for flexible or printed memory applications.<sup>[20–25]</sup> Active materials studied before include metal oxides (HfO<sub>2</sub>, ZnO, TiO, WSe, and others) as well as graphene and polymers (PMMA+MEH:PPV). Recently, also synaptic or analog printed memristors have been reported.<sup>[26–29]</sup> The majority of printed analog-type memristors for artificial synapses rely on modulation of conducting filaments within the active layer to achieve short- and long-term plasticity for spiking neural network implementations. Whilst it is challenging to realize short-term plasticity in those devices with time scales in the range of biological synapses, also other important concepts such as metaplasticity, signal integration, and temporal filtering has not been reported in printed memristors up to now. In particular for reservoir computing, memristor short-term plasticity has shown to be a feasible method for classification tasks at low required device amount.<sup>[32–34]</sup>

In this work, we present an inkjet-printed memristor, which can exhibit either interface-based, analog resistive switching for neuromorphic computing applications or filament-based, digital resistive switching for data storage applications. Both device properties are realized with only a single material composition, which allows for direct co-integration of digital and analog-type memristors on the same substrate at a low processing temperature of 120°C, which in the future can be used for flexible electronics. The device behavior can be adjusted by a suitable chosen electroforming voltage sweep or without using a forming voltage and exploitation of interface properties.

When used as filamentary-based, digital-type memristor, the device shows a low operation voltage with a SET voltage of 1.05 and -0.45V RESET voltage, an excellent endurance over 12 672

write and erase cycles, with a  $R_{\text{off}}/R_{\text{on}}$  ratio of  $10^2$ , and a retention of  $10^4$  s.

When used as an interface-based, analog-type memristor, the device exhibits synaptic behavior. For short-term plasticity, close to biological timescales are achieved for facilitation (10–177 ms), augmentation (10s), and potentiation (35s). Furthermore, the artificial synapse is thoroughly studied regarding its metaplasticity for memory formation and frequency dependent, non-linear signal integration and high-pass filtering capabilities, rendering it an ideal candidate for reservoir computing.

## 2. Results

### 2.1. Device Structure and Material Characterizations

The developed memristor is based on a three-material stack consisting of a laser-patterned gold (Au) bottom electrode, an inkjet-printed tungsten oxide (WO<sub>3-x</sub>) active layer, and an inkjet-printed silver (Ag) top electrode. As shown in Figure 1a, the effective area of the device is formed at the intersection of the two overlapping electrodes and is therefore defined by the overlapping area of the upper Ag top electrode (ca. 50 μm in width) and of the lower Au electrode (30 μm in width). The microscopic morphology of a pristine device is visualized in the cross-section depicted in the inset of Figure 1a by high-angle annular dark-field scanning transmission electron microscopy (HAADF-STEM), from which the thickness of each layer can be approximated (Au bottom electrode has a thickness of 100nm, inkjet-printed WO<sub>3-x</sub> active layer with a thickness of ca. 600nm and an inkjet-printed Ag top electrode of ca. 70nm). The elemental distribution of each layer is revealed by energy dispersive X-ray spectroscopy (EDS) over the red highlighted area, in which Ag, W, and Au are clearly traced in corresponding layers. The Pt layer above the Ag top electrode is utilized to protect the device structure during lamella preparation. Furthermore, we investigate the surface roughness of the inkjet-printed WO<sub>3-x</sub> active layer by atomic force microscopy (AFM) over an area of 1 μm × 1 μm. The AFM micrographs shown in Figure 1b reveal that the surface morphology of WO<sub>3-x</sub> layer consists of granular nanoparticles. The root mean square surface roughness is  $R_q = 28.90\text{nm}$ . In addition, scanning electron microscopic (SEM) images of inkjet-printed Ag and WO<sub>3-x</sub> can be seen in Figure S1a,b (Supporting Information).

To reveal the crystal phase composition of the inkjet-printed tungsten oxide, we investigate it with X-ray diffraction (XRD). From the obtained spectrum in Figure 1c, we observe a good match of the peaks in the measured XRD pattern with the data of the calculated WO<sub>3-x</sub> (ICSD84139) at the  $2\theta$  positions of 18.1° (002), 18.9° (110), 22.1° (102), 22.7° (012), and 26.0° (112). The (110) and (102) planes of the WO<sub>3-x</sub> crystalline can be clearly seen in the high-resolution transmission electron microscopic (HRTEM) image in Figure 1d with a lattice spacing of 3.65 and 3.14 Å, respectively. The inkjet-printed WO<sub>3-x</sub> layer is expected to consist of randomly oriented crystallites, which are revealed by the discrete scattered spots approaching a powder diffraction pattern in the selected area electron diffraction (SAED) image in the left half of Figure 1e. The right half of Figure 1e consists of the rotational average (upper part) extracted from experimental data and the simulated Debye rings (lower part) for WO<sub>3-x</sub>.

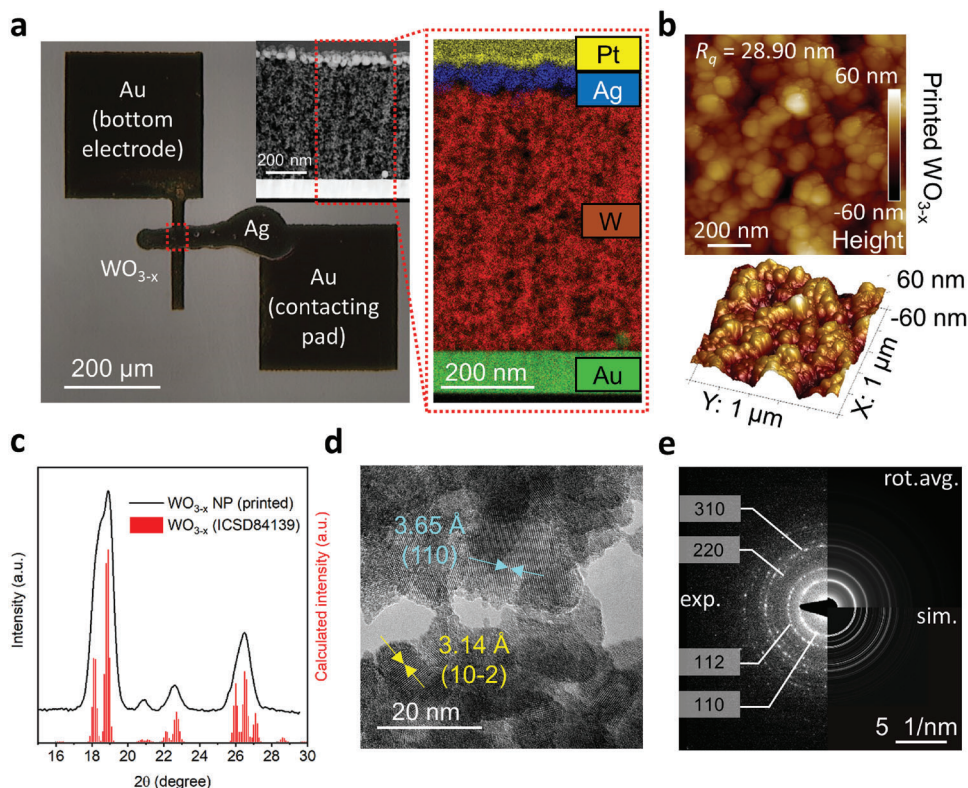


**Figure 1.** Device material characterizations. a) Optical image of the inkjet-printed memristor from a top view. The effective area of the device is formed at the overlapping area of top- and bottom- electrode, which is marked with a red dashed rectangle with a size of  $50\ \mu\text{m} \times 30\ \mu\text{m}$ . Inset: cross-sectional STEM HAADF micrograph of the inkjet-printed memristor. An EDS elemental map of selected area in STEM is shown in the zoom-in box. The elemental lines selected for the map are Pt\_L $\alpha$ , Ag\_K $\alpha$ , W\_L $\alpha$ , and Au\_L $\alpha$ . b) 2D and 3D AFM image of the inkjet-printed  $\text{WO}_{3-x}$  layer. c) XRD pattern of  $\text{WO}_{3-x}$ , inkjet-printed on Si wafer. For comparison, the calculated intensity of  $\text{WO}_{3-x}$  (ICSD84139) is plotted as red columns over  $2\ \theta$ . d) HRTEM image of  $\text{WO}_{3-x}$  layer. The planes indicated by the arrows can be assigned to  $\text{WO}_{3-x}$ . e) Experimental (exp.) SAED pattern of inkjet-printed  $\text{WO}_{3-x}$  layer (left half), rotational average (rot.avg.) of the experimental data (top right quadrant), and simulated (sim.). Debye rings for the  $\text{WO}_{3-x}$  (lower right quadrant).

Comparing the ring positions in Figure 1e, four prominent planes of  $\text{WO}_{3-x}$   $\{(310), (220), (112), \text{ and } (110)\}$  can be recognized from experimental data of printed  $\text{WO}_{3-x}$ . A rotational average pattern extracted from the SAED can be found in Figure S1c (Supporting Information), which is in good accordance with the XRD pattern, displayed in Figure 1c. In this work, the rotational averaging of the SAED pattern was performed with CrysTBox<sup>[35]</sup> and the simulation of Debye rings was done with Recipro.<sup>[36]</sup>

More information about the memristor fabrication workflow can be found in the Experimental Section and Figure S2 (Supporting Information).

## 2.2. Electrical Device Characteristics

Based on the applied voltage to the device, digital or analog resistive switching can be enabled. To achieve digital resistive switching, an initial electroforming process for the memristor is required (left-hand side of Figure 2a). Device electroforming is achieved by applying a positive voltage to the Ag top electrode whilst grounding the Au bottom electrode. This results in the formation of conductive Ag filaments within the  $\text{WO}_{3-x}$  active

layer as shown in Figure 2b. After filament formation, the device can be switched between two distinctive resistive states, namely the high resistive state (HRS) and the low resistive state (LRS) and shows typical bipolar resistive switching as sketched in the current-voltage ( $I$ - $V$ ) characteristics (Figure 2c). By alternately applying a positive (SET) and negative (RESET) voltage to the Ag top electrode the resistive state can be changed from HRS to LRS and vice versa. Both resistive states are maintained over an extended period of time when the applied voltage is removed (Figure 2d). This non-volatile resistive switching can be utilized for memory applications (Figure 2e).

To enable analog resistive switching, no electroforming is required over a pristine device and only negative voltages are applied to the device (Figure 2a). Applying a negative voltage to the Ag-based top electrode leads to the accumulation of oxygen vacancies ( $V_{\text{O}}$ ) at the Ag/ $\text{WO}_{3-x}$  interface (Figure 2f). The accumulated oxygen vacancies ( $V_{\text{O}}$ ) are used to modulate the height of the Schottky barrier and thus gradually change the conductivity of the device as schematically shown in Figure 2g. The volatile conductance over time (Figure 2h) can be exploited as artificial memristive synapse (Figure 2i) and furthermore shows non-linear integration and filtering behavior.

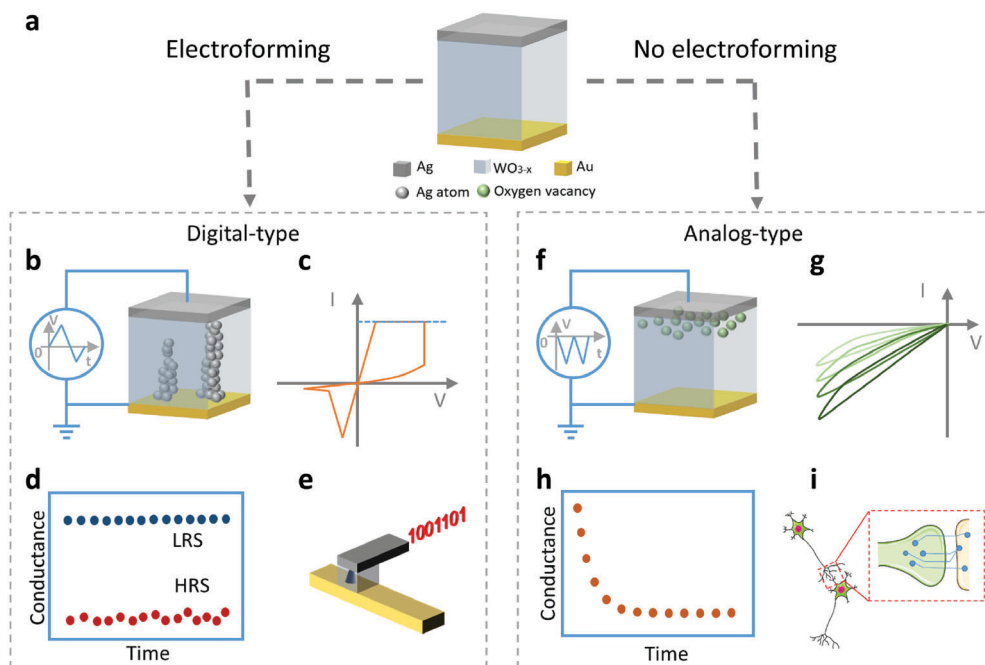


**Figure 2.** Schematic functional overview of the device behavior, which includes digital and analog resistive switching properties. a) The functionality is based on applying or not applying a prior electroforming voltage to a pristine device. To obtain a digital-type memristor, a positive electroforming voltage sweep is applied. This leads to formation of silver conducting filaments in the  $\text{WO}_{3-x}$  layer. If the device is intended to be used as analog-type memristor, no electroforming voltage is applied to the pristine device and only negative voltages are used to modulate the oxygen vacancies at the  $\text{Ag}/\text{WO}_{3-x}$  interface. For digital-type memristor: b) Resistive switching is ascribed to the formation and rupture of Ag conducting filaments. c) Schematic  $I$ - $V$  characteristics of the digital-type device. d) Conductance/resistive states of digital-type device are stable over time showing its non-volatility. e) Digital-type device can operate as a non-volatile memory cell for digital information storage. For analog-type memristor: f) Concentration change of oxygen vacancies at the  $\text{Ag}/\text{WO}_{3-x}$  interface accounts for the analog resistive switching. g)  $I$ - $V$  characteristic of the analog-type device. h) Obtainable increased conductance is volatile and decreases exponentially with time. i) Volatile analog resistive switching behavior allows the memristor to function as an artificial-synapse, which can be used in neuromorphic computing. The schematic of a synapse in **Figure 2h** was modified based on the template from Servier Medical Art by Servier, which is licensed under a Creative Commons Attribution 3.0 unported license.

In the following, the  $\text{Ag}/\text{WO}_{3-x}/\text{Au}$  device is investigated in terms of its digital and analog resistive switching performance. For all voltage-dependent investigations, the voltages are applied at the Ag top electrode, whilst the Au bottom electrode remains grounded, if not further mentioned. Also, for all reported voltage sweeps, the voltage step size for the forward sweep is 0.01 and 0.1V for the backward sweep.

### 2.3. Digital-Type Memristor Characterization

To determine the digital resistive switching behavior of the developed device, an initial voltage sweep ( $0\text{V} \rightarrow 5\text{V}$ ) is applied over a pristine memristor, to build the initial conducting filaments within the  $\text{WO}_{3-x}$  layer (see **Figure 3a**). At 4V, the measured current abruptly reaches the compliance current (CC) of 0.8mA, which indicates the initial electroforming voltage of the digital-type memristor.

After the initial electroforming process, the device is switched between its LRS and HRS by consecutive positive and negative voltage sweeps. It should be noted, that the SET voltage is much lower than the initial electroforming voltage, due to the residual conducting filaments, which were prior formed in the  $\text{WO}_{3-x}$

layer. For further reading, this process is visualized in **Figure S4** (Supporting Information). For the SET process, a voltage sweep ( $0\text{V} \rightarrow 2\text{V} \rightarrow 0\text{V}$ ), is applied over the device, with a CC of 0.8mV. To RESET the memristor, a voltage sweep ( $0\text{V} \rightarrow -1\text{V} \rightarrow 0\text{V}$ ) without CC is used. **Figure 3a,b** shows 11 representative  $I$ - $V$  curves from 100 consecutive sweeping cycles. The full 100 sweeping cycles and corresponding resistances are shown in **Figure S3** (Supporting Information). For cycle-to-cycle device investigation, the distributions of the obtained 100 SET and RESET voltages are depicted as histograms in **Figure 3c**. The obtained memristor SET voltage shows a low mean value of  $\bar{x} = 1.05\text{V}$ , with a standard deviation of  $s = 0.29\text{V}$ . The RESET voltage is centered around a mean value of  $\bar{x} = -0.45\text{V}$  with a standard deviation of  $s = 0.11\text{V}$ .

To investigate the retention performance of the device, the resistances of both resistive states are plotted in **Figure 3d** over  $10^4$  s. Therefore the device is set to a defined resistive state (HRS or LRS), and its resistive state is continuously obtained by a read voltage, with a pulse height of 0.01V and width of 200 ms. As visualized, both resistive states remain stable over the investigated time and no signs of obvious degradation can be observed. The retention performance of the device further highlights its potential as a non-volatile memory element.

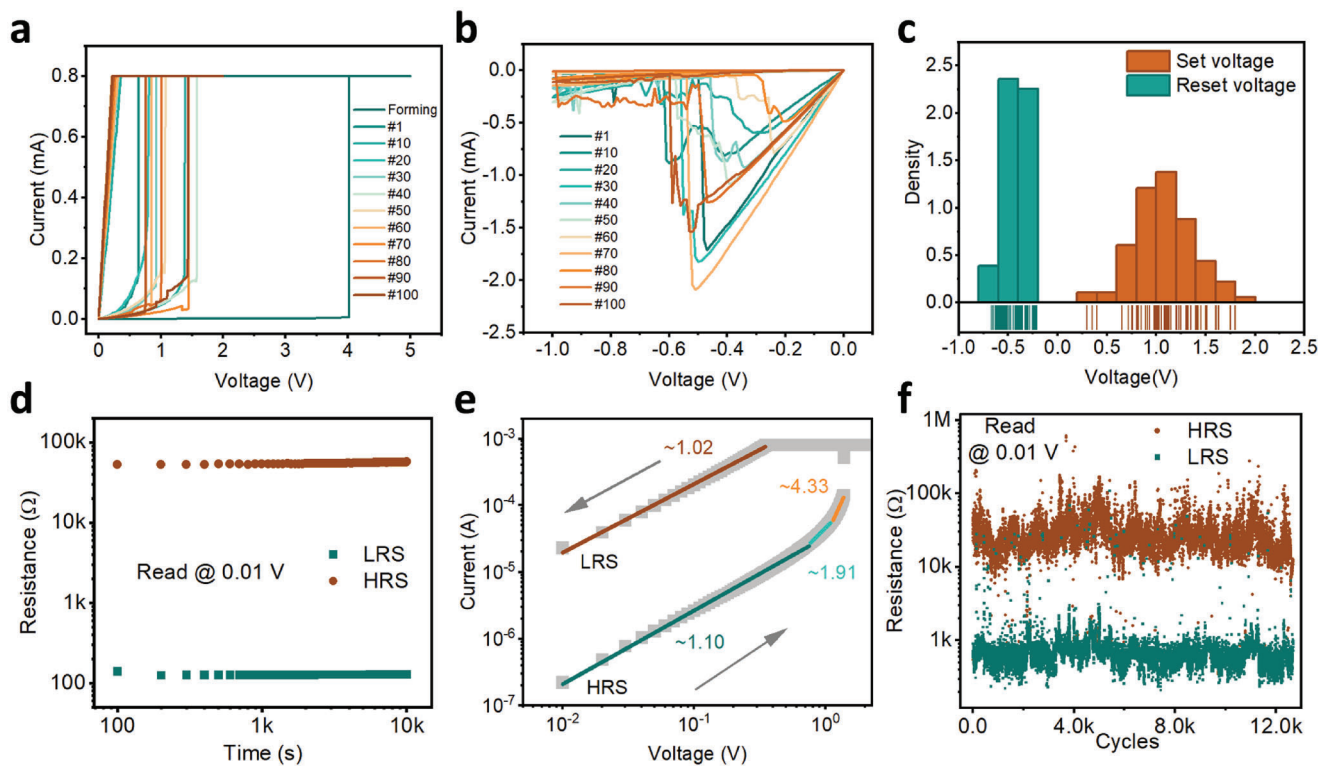


**Figure 3.** Digital resistive switching characteristics. a)  $I$ - $V$  curves of the electroforming voltage sweep and 11 SET processes (out of 100) with a compliance current of 0.8 mA. For the electroforming process, the voltage sweep is performed from 0V  $\rightarrow$  5V  $\rightarrow$  0V. The sweeping voltage range for the SET process is 0V  $\rightarrow$  2V  $\rightarrow$  0V. b)  $I$ - $V$  curves of 11 RESET processes. Here, the voltage is swept from 0V  $\rightarrow$  -1V  $\rightarrow$  0V. c) Distribution of SET and RESET voltage values extracted over 100 switching cycles, visualized as histograms. d) Device retention of the HRS and LRS over 10<sup>4</sup> s. e)  $I$ - $V$  curve of the SET process at logarithmic scale. The arrows indicate the voltage sweeping direction. f) Endurance performance of the memristor, operated under pulse mode.

### 2.3.1. Conduction Mechanism

In the following, we investigate the conduction mechanism of the digital-type memristor. The  $I$ - $V$  curve, of the SET process is plotted on a double-logarithmic scale. The linear fit of the slopes of the measured curves for different resistive states and at various voltage ranges are compared, as shown in Figure 3e. In the case of the HRS, the conducting filaments (CF), which consist of silver atoms, are ruptured. Thus, a gap is formed between the top electrode and the “virtual” electrode of the residual silver CF, formed in the tungsten oxide layer, which is considered as an extension of the Au bottom electrode. When the positive voltage at the top electrode is gradually increased, primarily a minuscule amount of charge carriers in the active layer are thermally excited and lead to Ohmic conduction in the low field regime.<sup>[37]</sup> Correspondingly, the slope of the HRS at low voltage and current values is 1.10, as shown in Figure 3e. As the applied voltage continuously increases, electrons from the residual conducting filaments fill the traps in the gap of the tungsten oxide until they are completely filled. This process is shown in Figure 3e, as an increase in the slope from 1.91 to 4.33 in the HRS curve can be observed. This fits with the theory of space charge limited conduction (SCLC).<sup>[38]</sup> The SCLC theory is further classified into two types. The type with unfilled traps obeys Child’s square law with  $I \propto V^2$ , while the type with filled traps leads to an exponential in-

crease in the current.<sup>[38]</sup> As shown in Figure 3e, a huge increase in current can be observed, which matches trap-filled SCLC theory, and indicates a re-connection of the residual CF to the top electrode. For the LRS curve, the slope value is 1.02, which is in accordance with Ohm’s law and indicates the existence of a metallic contact between the two electrodes. The process of filament formation, rupture, and re-connection of the studied device is shown schematically in Figure S4 (Supporting Information) and explained in detail in Note S1 (Supporting Information).

### 2.3.2. Dynamic Performance for Memory Applications

To investigate the performance of the memristor as a non-volatile memory device, voltage pulses are applied to the device for 200ms to switch between the resistive states. For the “write” operation, which sets the device to LRS a voltage pulse of 3V and a CC of 800  $\mu$ A is used, while a voltage pulse of -1.5V is used for the “erase” operation, which resets the device to HRS, without any CC. After each “write” and “erase” cycle, the resistance is read out through a small voltage pulse of 0.01V. Figure 3f shows the results after “writing” (blue dots) and “erasing” (red dots) the device over 12 672 cycles. Only a few switching events fail, and a resistance  $R_{\text{off}}/R_{\text{on}}$  ratio of 10<sup>2</sup> is obtained. In Figure 3f, the endurance cycle-to-cycle variability of the HRS and LRS is observable, which

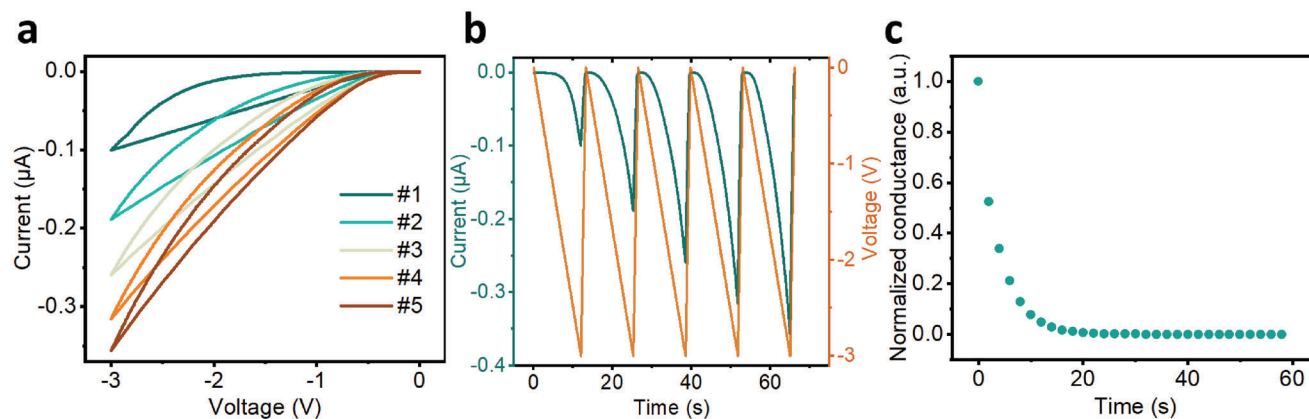


**Figure 4.** Analog resistive switching device. a)  $I$ - $V$  characteristics measured over five consecutive DC voltage sweeps ( $0 \rightarrow -3 \rightarrow 0$  V), which show the gradual increase of conductivity. b) Applied voltage and measured current over time. c) Exponential decay of the normalized conductance of the device over time, which is measured after the fifth voltage sweep. This indicates the volatility of the conductance when the applied voltage is removed.

is a common effect in EMC-based memristors due to their intrinsic stochastic properties.<sup>[39]</sup> If necessary, the endurance uniformity can be optimized by suitable circuit architectures, such as 1-transistor 1-memristor (1T1R) and feedback algorithms with adaptive current compliance measures.<sup>[40,41]</sup>

#### 2.4. Analog-Type Memristor Characterization

To exploit the interface-based, analog resistive switching of the device, no initial electroforming voltage and only negative voltage sweeps and pulses are used to avoid Ag filament formation within the active layer. The gradual increase in conductivity of the memristor is shown in **Figure 4a**, by applying five consecutive negative voltage sweeps ( $0\text{V} \rightarrow -3\text{V} \rightarrow 0\text{V}$ ), over the device. To visualize the dynamic incremental conductivity change with multiple successive negative voltage sweeps, the voltage and current are plotted over time in **Figure 4b**. The peaks, observed in the current measurements, increased steadily with each voltage spike, which is similar to the increase in efficacy of a biological synapse, exposed to a continuous stimulus. This analog resistive switching can be exploited for the development of an artificial memristive synapse.<sup>[42]</sup>

The gradual increase in conductivity of the inkjet-printed memristor is due to the continuous accumulation of oxygen vacancies at the Ag/ $\text{WO}_{3-x}$  interface, as tungsten oxide is an  $n$ -type transition metal oxide-based semiconductor, where oxygen vacancies ( $V_{\text{O}}$ ) act as dopants that increase the overall conductivity. The metal/semiconductor interface properties can be dynamically adjusted, by changing the amount of oxygen or oxygen vacancies ( $V_{\text{O}}$ ).<sup>[43-47]</sup> Therefore, gradually tunable resistive switching can be achieved, by applying an external electrical field to the device, which helps to manipulate the amounts of oxygen vacancies ( $V_{\text{O}}$ ) in the tungsten oxide. For more information about the underlying physical and chemical mechanisms see Note S2 and **Figure S5** (Supporting Information).

For the analog-type memristor, the conductance decreases over time, due to the volatility of the migrated oxygen vacancies. As shown in **Figure 4c**, an exponential decay of the normalized conductance is observed, after the device experienced five consecu-

tive voltage sweeps. This can be attributed to the restoration of the Schottky-like contact at the Ag/ $\text{WO}_{3-x}$  interface, caused by the spontaneous diffusion of the oxygen vacancies away from the metal/semiconductor interface. This conductance decay also explains the overlapping hysteresis loops in **Figure 4a**. The phenomenon of volatile resistive switching in the reported inkjet-printed memristor can be used to emulate synaptic plasticity, which refers to the modification of the strength of synaptic transmission between two neurons.<sup>[48]</sup>

In the following, we investigate the inkjet-printed memristor's capabilities as an artificial synapse for neuromorphic applications over different forms of synaptic short-term plasticity. Furthermore, we investigate the frequency-dependent signal processing capabilities of the artificial synapse.

##### 2.4.1. Artificial Memristive Synapse: Paired-Pulse Facilitation

In a biological synapse (**Figure 5a**, upper part), when two action potentials in rapid succession depolarize the pre-synaptic neuron, the second action potential can release more neurotransmitters than the first one, resulting in multiple times higher post-synaptic current (PSC).<sup>[49]</sup> This biological phenomenon is called paired-pulse facilitation (PPF),<sup>[48-51]</sup> and is described for biological synapses by the residual calcium ( $\text{Ca}^{2+}$ ) theory.<sup>[51]</sup> Facilitation in biological synapses can persist for tens to hundreds of milliseconds and is considered as an important factor in the encoding of temporal information.<sup>[52]</sup>

The paired-pulse facilitation (PPF) is emulated with the presented inkjet-printed artificial memristive synapse, by applying two identical voltage pulses and measuring the output current, induced by these two successive voltage pulses within a short time interval (see **Figure 5a**). The corresponding results for the artificial memristive synapse are shown in **Figure 5b**, where successive voltage pulses of  $-5\text{V}$  are applied to the device over 10ms. The interpulse interval ( $\Delta t$ ), which is the duration of the pulse-off time, is 30ms. It can be observed, that the second evoked current ( $I_2$ ) exceeds the first ( $I_1$ ), which is similar to the facilitation observed in biological synapses. As discussed earlier, this effect can be explained by oxygen vacancies in the tungsten oxide

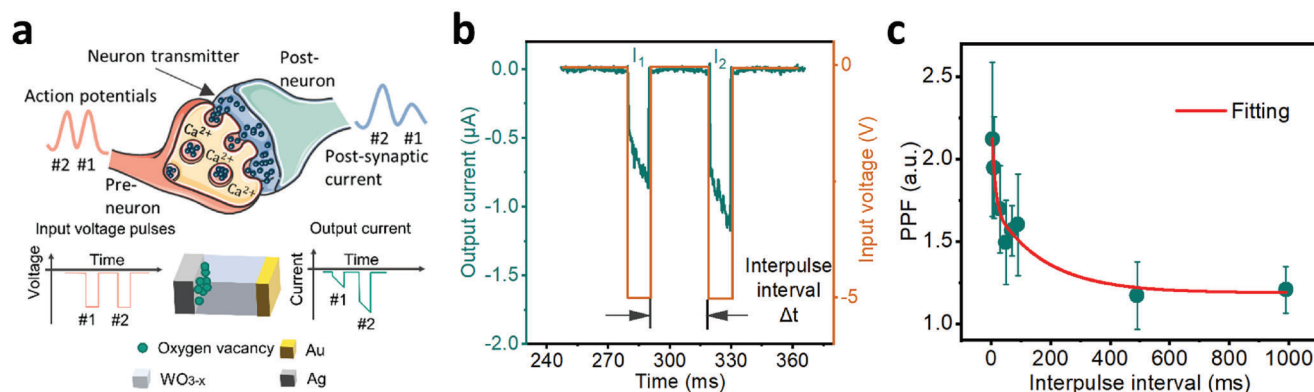


**Figure 5.** Paired-pulse facilitation (PPF) of the artificial memristive synapse. a) Schematic illustration of PPF in a biological synapse and emulation of the PPF using our memristor. b) Experimental result of the inkjet-printed memristor by applying two consecutive identical voltage pulses. The second evoked current  $I_2$  is higher than the initial current  $I_1$  response. c) Measured decay of the PPF with increasing time intervals between voltage pulses. The green dots are the obtained mean values. The error bar indicates the standard deviation. The fit of the exponential decay curve was obtained using Equation (2). The schematic of the synapse in Figure 5a was modified, based on the template from Servier Medical Art by Servier, which is licensed under a Creative Commons Attribution 3.0 unported license.

active layer, which migrate along the electrical field and accumulate near the Ag top electrode. This reduces the height of the Schottky barrier between the silver top electrode and the tungsten oxide, which leads to increased conductivity of the device. This effect has been recently observed also in other material systems (Pt/WO<sub>3-x</sub>)<sup>[53]</sup> and other semiconductors.<sup>[44,47,54]</sup> Analogous to the residual Ca<sup>2+</sup> theory, the migration and accumulation of the oxygen vacancies, triggered by the first input voltage pulse, contribute to the increase in the conductivity produced by the second stimulus. Therefore, the interpulse interval needs to be shorter than the spontaneous diffusion time of the oxygen vacancies, which would counteract the accumulation and therefore the conductivity increase.

The synapse-like current enhancement, observed in the memristor can be quantified by the following equation:<sup>[50]</sup>

$$\text{PPF} = \frac{I_2}{I_1} \quad (1)$$

where  $I_1$  and  $I_2$  represent the PSC measured from the memristor and caused by the first and the second voltage pulse, respectively.

Based on the residual Ca<sup>2+</sup> theory, the magnitude of the PPF is supposed to decrease with increasing interpulse interval  $\Delta t$ .<sup>[51,55]</sup> To emulate this interpulse-dependent decay in PPF for our artificial memristive synapse, paired-pulses with identical height (-5V) and width (10ms), with varying interpulse interval, are utilized to stimulate the device. The interpulse intervals are set to  $\Delta t = \{5, 10, 30, 50, 70, 90, 490, 990\}$  ms, respectively. The paired pulses of each interpulse interval are applied five times over the same memristor. The PPF is calculated using Equation (1), for each aforementioned varying interpulse interval and plotted above the mean values in Figure 5c, including error bars, which indicate the standard deviation of the sample.

To describe the decreasing trend of the PPF with increasing interpulse interval, observed in the memristor, a double exponential decay function<sup>[50,56]</sup> is modified in the following form:

$$\text{PPF} = A + C_1 e^{(-\Delta t/\tau_1)} + C_2 e^{(-\Delta t/\tau_2)} \quad (2)$$

where  $\Delta t$  is the interpulse interval,  $C_1$  and  $C_2$  are the enhancement magnitudes of the rapid and slow facilitation phases, whilst  $\tau_1$  and  $\tau_2$  represent the characteristic relaxation time of the two facilitation periods.<sup>[50]</sup> The parameter  $A$  is utilized to adjust the fitting results.

The PPF over the interpulse interval is fitted as a red curve over the measured mean values and plotted in Figure 5c, corresponding to the double exponential decay function from Equation (2). The red curve in Figure 5c shows facilitation with two components. It includes a fast decaying phase with  $\tau_1 = 10\text{ms}$  and  $C_1 = 0.68$ , as well as a slow decaying phase with  $\tau_2 = 177\text{ms}$  and  $C_2 = 0.54$ . The characteristic relaxation time constant of the two decaying phases is similar to the time scale of many biological synapses.<sup>[50]</sup> According to the fitting result, the parameter  $A$  in the modified double decay function Equation (2) is 1.19, which slightly deviates from the value of 1 for biological synapses.<sup>[50]</sup> From the PPF results, we can observe, that our inkjet-printed artificial synapse is capable to emulate biological synapses.

#### 2.4.2. Artificial Memristive Synapse: Short-Term Plasticity with Enhanced Relaxation Time for Memory formation

In the following, we examine longer-lasting forms of synaptic plasticity, such as potentiation. This is achieved by repeated, prolonged application of input stimuli trains between 200ms and 5s.<sup>[50]</sup> Potentiation is referred to as activity-evoked enhancement for a synaptic connection that can maintain synaptic efficacy over extended periods of time. Typical time spans are in the range of tens of seconds or even several minutes.<sup>[57]</sup> In addition to potentiation, another form of synaptic plasticity exists. If the activity-induced synaptic enhancement decays within a few seconds, it is referred to as augmentation.<sup>[58]</sup>

The following experiments are designed to reconstruct the dynamic process that occurs at a post-synaptic neuron after the pre-synaptic counterpart is exposed to different amounts of repetitive stimulation. Through these experiments, different forms of synaptic short-term plasticity and memory formation in a



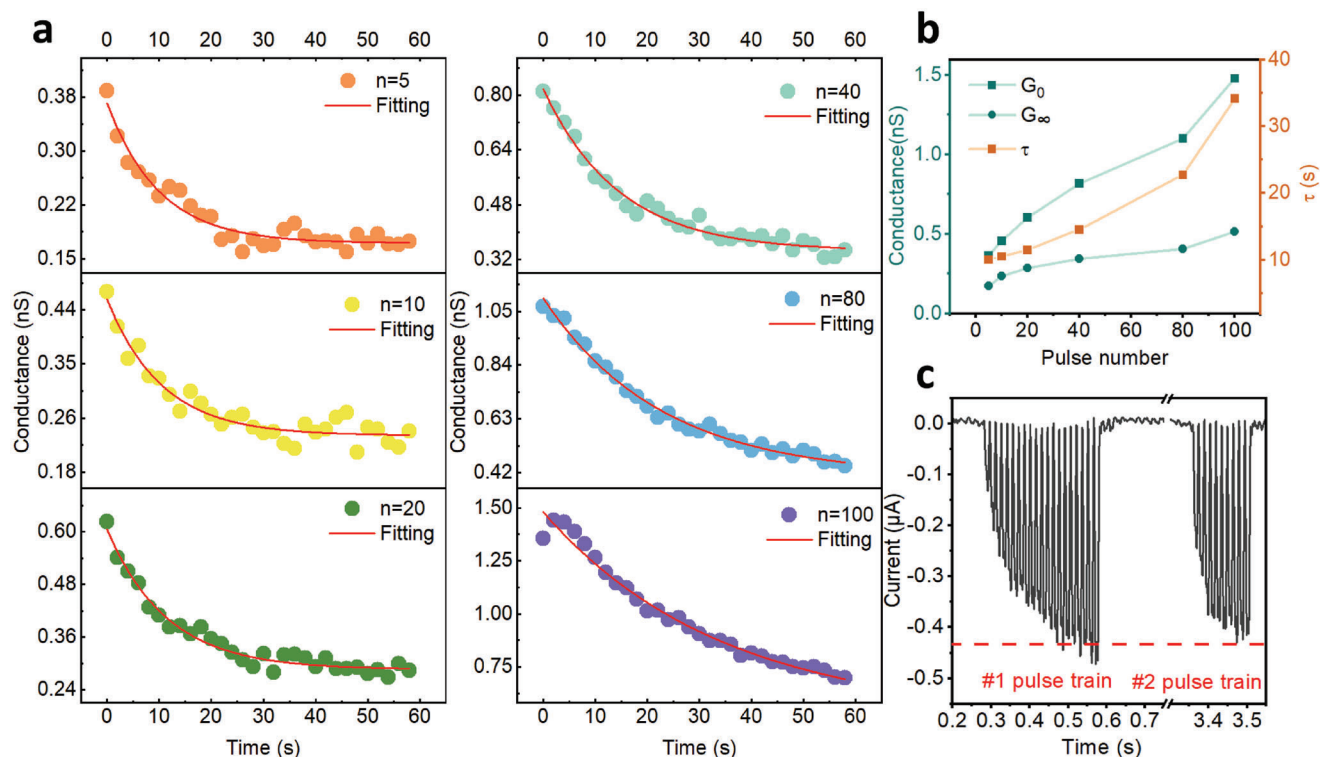


**Figure 6.** Memory formation process of the artificial memristive synapse. a) Conductance decay after stimulation by various numbers of the voltage pulse, ( $n = \{5, 10, 20, 40, 60, 100\}$ ). The conductance decay is fitted using Equation (3). b) Extracted time constants ( $\tau$ ) and conductance enhancement ( $G_0$ ,  $G_\infty$ ) from Equation (3). c) Current responses of two voltage pulse trains. The first voltage pulse train requires 20 pulses to reach the threshold value (red dashed line), whereas for the second voltage pulse train only 10 pulses are needed to reach the threshold value. The measured results indicate a faster learning process of the memristor after training.

biological synapse are emulated by our inkjet-printed memristor. Therefore, the device is repeatedly stimulated with different amounts ( $n = \{5, 10, 20, 40, 80, 100\}$ ) of negative voltage pulses with identical width (20 ms), height (-5V), and interpulse intervals (20 ms). The waveform of the voltage pulse is shown in Figure S6 (Supporting Information).

Immediately after the last input voltage pulse, the conductivity of the device is read out, by measuring its resistance. This is done every 2s with a small voltage pulse of 0.01V over 200 ms. The change in conductance is visualized over time in Figure 6a to reveal various relaxation characteristics after different amounts of stimuli. To gain insight into the conductance decay behavior, the following equation is used to fit the obtained results. The form of the equation is derived from an exponential function, used to describe the relaxation phenomena in biological synapses and in oxide materials (A discussion in detail can be found in Note S3, Supporting Information). The modified equation is written as:

$$G(t) = (G_0 - G_\infty) \cdot e^{-(t/\tau)^\beta} + G_\infty \quad (3)$$

where  $t$  is the time, recorded after the last voltage pulse applied to the device,  $G(t)$  is the conductance at  $t$ ,  $G_0$  is the transient conductance immediately after the last input voltage pulse. Furthermore,  $G_\infty$  describes the stabilized conductance at infinite time,  $\tau$  is the characteristic relaxation time constant, indicating how fast

conductance declines to  $1/e$  of  $G_0$ , and  $\beta$ , ranging from 0 to 1, is considered as the stretching index to adjust the curve for better fit.<sup>[59]</sup> In the case of the inkjet-printed memristor, reported in this work, the conductance relaxation is adequately described when  $\beta$  is set to 1 in Equation (3) (red solid line in Figure 6a). Since the exponent  $\beta$  is related to the degree of correlation of the ion transport, the value of 1 indicates random Debye-like hops of oxygen vacancies away from the silver electrode, when the voltage over the device is removed.<sup>[60]</sup>

As mentioned earlier, synaptic short-term plasticity of different forms can be distinguished by the relaxation time constant. When  $\tau$  is extracted from the fitted curves in Figure 6a and plotted over the corresponding pulse number in Figure 6b, an increase in the time constant from 10 to 35s with increasing pulse number is obtained. The extracted time constants of the inkjet-printed memristor coincide with reported values for augmentation (ca. 7s) and potentiation (ca. 30s) in biological synapses.<sup>[61]</sup> From a neurobiological point of view, prolonged stimulation (more stimuli when pulse width and frequency are fixed) leads to an augmented release of  $\text{Ca}^{2+}$ , resulting in a longer time that is needed to remove the residual  $\text{Ca}^{2+}$ . In the case of the memristor, oxygen vacancies behave similarly to  $\text{Ca}^{2+}$ . As more oxygen vacancies are forced to migrate to the top electrode with increasing numbers of input voltage pulses, the increased conductivity at the metal/semiconductor interface will decay slower. This stimulus number-dependent relaxation in the memristors can be seen

in Figure S6 (Supporting Information), when  $G(t)$  is normalized over  $G_0$  and visualized over time.

As introduced previously,  $G_0$  and  $G_\infty$  represent the transient conductive state and equilibrium conductive state, at  $t = 0$  and  $t = \infty$ , respectively. Both values can be extracted from Equation (3), when fitted over the results, as shown in Figure 6a. The obtained values are plotted over the pulse numbers in Figure 6b. By increasing the number of input pulses,  $G_0$  increases to a larger extent than  $G_\infty$ . This leads to a higher activated amplitude  $G_0 - G_\infty$ , which accounts for the longer relaxation time constant ( $\tau$ ), shown in the same figure. The level  $G_\infty$  in Figure 6b is consistently elevated by increasing the number of voltage pulses, which reveals a permanent increase of the conductivity in the memristor. The permanent conductance enhancement of the device is due to the stoichiometric changes of oxygen in the tungsten oxide active layer near the top electrode, caused by trapped oxygen vacancies. In neuroscience, a similar concept has been proposed to explain memory formation in the brain, which states structural changes in the synaptic morphology, known as “engram”, underlying newly formed memory.<sup>[62,63]</sup>

Inspired by neuroscience, we can observe a “memory” effect at the tungsten oxide layer near the top electrode after repeated stimulation of voltage pulses, due to reduced oxygen concentration in this area. This induced “memory” from structural changes and residual oxygen vacancies, right after the release of the voltage pulse train, can jointly modulate the behavior of the device as shown in Figure 6c. Primarily, a train of 20 voltage pulses of identical width, height, and time interval is applied to the Ag top electrode of an unformed memristor and the induced current is measured. More details are shown in Experimental Section. After letting the device “rest” for several seconds, it’s stimulated again with a pulse train incorporating the same parameters as the primary one, but this time using only 10 consecutive pulses. As visualized in Figure 6c, the current evoked by each voltage pulse of the second stimulation train is largely increased, in comparison to the primary pulse train, which indicates a faster and easier enhancement of the second group of repetitive stimuli. In this case, the subsequent plasticity of the memristor is modulated by the previous “activity-experience”, which is labeled in neuroscience as metaplasticity.<sup>[64]</sup> Metaplasticity is regarded as a key property of a biological synapse that can address catastrophic forgetting, which means the previous learning contents are rapidly overwhelmed during the training for a new task.<sup>[65]</sup> By mimicking the metaplasticity of a synapse, several reported artificial networks are capable to perform better learning tasks.<sup>[65–67]</sup> From the obtained measurement results of our artificial memristor synapse, we observe plasticity as well as metaplasticity with excellent time scales close to biological synapses. The reported characteristics suggest the device’s capabilities for neuromorphic computing.

#### 2.4.3. Artificial Memristive Synapse: Frequency Dependent input Signal Filtering and Integration

The earlier introduced experiments were able to show that the printed memristors can resemble important synaptic short-term plasticity properties regarding information storage and memory formation. Next to the reported figures of merit, further important synaptic properties exist in biological synapses, such as sig-

nal filtering and integration.<sup>[48,68–70]</sup> This synaptic signal processing capabilities can provide an important building block for artificial neural network circuits, in order to increase the accuracy.<sup>[69]</sup>

In the following, we further investigate the capabilities of our inkjet-printed memristor to emulate synaptic short-term plasticity related signal processing features, such as filtering and integration with respect to facilitation. For the experiments, ten consecutive, identical voltage pulses, as shown in Figure 7a, are applied to the memristor to mimic the input signal burst, at a biological synapse. The output voltages are obtained over an additional resistor. The measurement setup is fully described in Experimental Section. The height of the input voltage pulse waveform is -5V and is applied over 10ms, while the interpulse time interval is varied to achieve several frequencies of 2, 10, 25, and 67Hz.

Figure 7b displays the output voltage response with respect to the input voltage pulse train over different frequencies. From the obtained measurements, we can observe high-pass filtering and integration behavior in the inkjet-printed device. Although the pulse potential and pulse duration were kept the same, a difference in the output potential is observable, which is similar to the behavior of a biological synapse with a low initial release function.<sup>[48]</sup>

The experiments show, that with increasing input pulse frequency an increased output potential can be measured. The non-linear integration tendency is observable at input frequencies of 10, 25, and 67Hz (see Figure 7). From 25Hz and beyond, the voltage levels saturate at a plateau of  $\approx 0.42V$ , due to oxygen vacancy saturation at the metal/semiconductor interface. At a low input signal frequency of 2Hz, no increase in voltage (efficacy) is observable. Here, the voltage levels are not integrated by the artificial synapse, which resembles the behavior of a biological synapse with a low initial probability of release function.<sup>[48]</sup> The observed filtering and integration capability can be explained by the electrical attraction of the positively charged oxygen vacancies ( $V_O$ ) toward the Ag top electrode when applying negative voltage pulses. This reduces the resistance of the device, due to the Schottky barrier lowering. As a result, the voltage drop on the voltage measurement resistor will gradually increase. However, after a certain amount of successive voltage pulses, the conductivity at the Ag/ $WO_{3-x}$  interface cannot increase further, which results in a saturation of the voltage level. This can be explained by a change in the oxygen vacancies ( $V_O$ ) concentration gradient at the metal/semiconductor interface during operation. Therefore, the first voltage pulses can shift the oxygen vacancies ( $V_O$ ) concentration easier than the later ones, which accounts for the saturated output voltage, shown in Figure 7b. Furthermore, since the movement of oxygen vacancies is defined by the on-and-off period of the input voltage pulse train, the cumulative enhancement of the conductivity is frequency-dependent. The higher the frequency of the input signals, the less time will be left for the device to “relax” between two voltage pulses, which leads to higher integration of the output voltage, within a certain number of consecutive input voltage pulses.

The reported artificial synapse is capable to filter unnecessary, low-frequency information of 2Hz and shows frequency dependent, non-linear integration capabilities at frequencies of 10, 25, and 67Hz. This synaptic signal processing feature of the device can be beneficial in artificial neural network circuits.

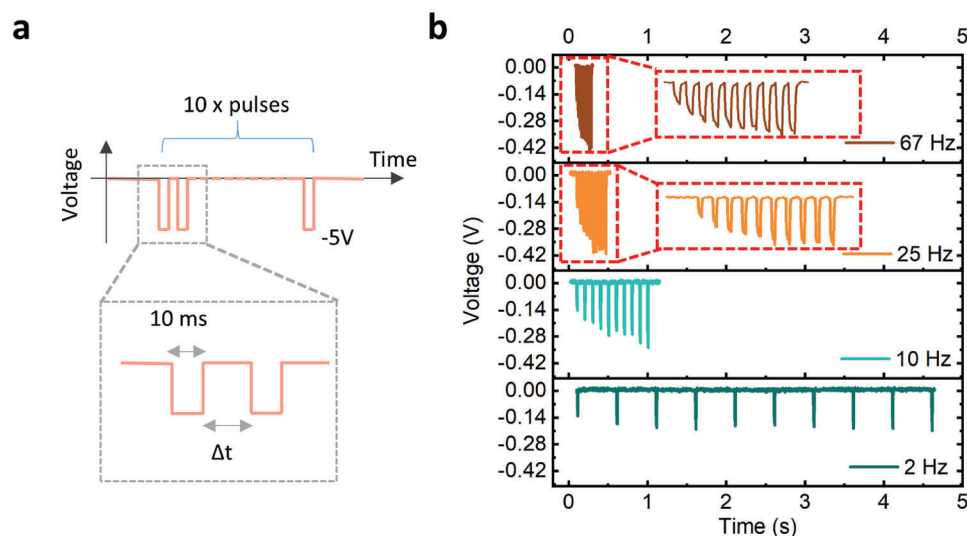


**Figure 7.** Frequency dependent integration of input signals. a) Waveform of the applied input voltage pulse train over the inkjet-printed memristor. The voltage amplitude and pulse-on time of a single voltage pulse are  $-5\text{V}$  and  $10\text{ms}$ . Various interpulse intervals can produce different frequencies, ranging over 2, 10, 25, and  $67\text{Hz}$ . b) Output voltage of the memristor, as a response to the input voltage pulse train for different frequencies.

### 3. Discussion

In this work, we present an inkjet-printed memristor based on an  $\text{Ag}/\text{WO}_{3-x}/\text{Au}$  material stack and investigate its capabilities for non-volatile memory as well as neuromorphic computing applications. By the formation of a conducting silver filament within the utilized tungsten oxide layer, the device sub-sequentially can be operated as a digital-type memristor, which can be switched between a low- and high-resistive state for efficient digital information storage. The digital-type memristor enables low-voltage operation with a SET voltage of  $1.05\text{V}$  and a RESET voltage of  $-0.45\text{V}$  and a resistive switching ratio  $R_{\text{off}}/R_{\text{on}}$  of  $\approx 10^2$ . The device retention is investigated over a time span of  $10^4\text{ s}$  with no obvious sign of degradation. Regarding the dynamic device performance, the inkjet-printed device shows stable endurance of over 12 672 write and erase cycles. The reported endurance switching cycles are the, up to now, highest among compared to all other printed memristors published in recent years. A comparison is shown in Table S1 (Supporting Information). The device's conduction mechanism is investigated and fits trap-controlled SCLC theory.

To enable analog resistive switching with the reported inkjet-printed memristor, no initial electroforming voltage is required. By operating the device with only negative voltages, volatile analog resistive switching is achieved. The dynamic transition between Schottky- and Ohmic-like contact at the  $\text{Ag}/\text{WO}_{3-x}$  interface, which is caused by the stoichiometric change of oxygen in the tungsten oxide semiconductor, causes conductance plasticity of the device. As a consequence, our reported device is able to emulate functions of biological synapses, such as short-term plasticity and memory formation after repeated stimulation. Extended electrical characterization of the device was performed and compared to biological functions. This includes paired-pulse facilitation for temporal information coding, as well as potentiation and augmentation for memory formation. The device exhibits intrinsically close to biological signal timescales. This includes facil-

itation ( $10\text{--}177\text{ms}$ ), augmentation ( $10\text{s}$ ), and potentiation ( $35\text{s}$ ). The results show, that our inkjet-printed artificial synapse is well suited for the emulation of biological synapses. Furthermore, the short-term plasticity signal processing capabilities of the artificial synapse were studied by frequency-dependent integration of input-train stimuli. The results show, that the device can serve as a high-pass filter for low-frequency signal suppression ( $2\text{Hz}$ ) and as a non-linear signal integration element at frequencies from  $10\text{Hz}$  and upward. The aforementioned figures of merit in emulating short-plasticity of the biological synapse are rarely reported in other printed memristive devices (see Table S2, Supporting Information).

The inkjet-printed memristor reported in this work can successfully achieve digital information storage and neuromorphic-like learning and signal processing capabilities. These multimodal features can be utilized to enable novel circuit design paradigms in printed electronics for near-sensor computing, and wearable electronics.

### 4. Experimental Section

**Device Fabrication:** For inkjet-printing, a drop-on-demand piezo inkjet-printer was used (DMP2831, Fujifilm). The gold bottom electrode of the device was a  $30\mu\text{m}$ -wide bar patterned by laser ablation on commercially available gold-coated glass (Sigma-Aldrich, thickness  $100\text{nm}$ ) using a Trumpf TruMicro 5000 ps laser. The patterned bottom electrodes were sonicated at room temperature over  $15\text{ min}$  in a mixed solution of isopropanol and acetone (ratio of 1:1 in volume). The  $\text{WO}_{3-x}$  nanoparticle ink (Sigma-Aldrich) was inkjet-printed onto the patterned gold bottom electrode.

After printing of the  $\text{WO}_{3-x}$  layer, the sample was annealed at  $120^\circ\text{C}$  over  $1\text{ h}$  in a furnace to eliminate the residual solvents. For the top electrode, an Ag nanoparticle ink (Silverjet DGP, Sigma-Aldrich) was inkjet-printed onto the  $\text{WO}_{3-x}$  layer vertically to build a crossing junction with the bottom electrode and subsequently annealed at  $120^\circ\text{C}$  for  $1\text{ h}$  to obtain a good conductivity. The whole fabricating process was graphically described in Figure S2 (Supporting Information).

**Cross-Section Preparation:** To prepare the cross-sectional sample, the Memristor structure on glass was first sputtered with 5nm Pt, using a Leica ACE600 sputtercoater. The device of interest was localized using SEM in a FEI Strata 12672S DualBeam FIB-SEM. To protect the thin film during lamella preparation, a protective platinum layer of  $20\mu\text{m} \times 2\mu\text{m} \times 0.1\mu\text{m}$  was deposited by electron beam induced deposition (EBID) and subsequently a slightly larger patch with height of  $4\mu\text{m}$  was deposited by ion beam induced deposition (IBID). Trenches close to the protective Pt patch were milled by 30kV Ga-ions on both sides of the tentative lamella. Then, the pre-thinned lamella was cut free, welded to the tip of an Omniprobe manipulator and attached to an Omniprobe copper grid. In a final step the lamella was thinned from the initial thickness of ca.  $3\mu\text{m}$  down to electron transparency ( $<100\text{nm}$  thickness) by Ga-ions with energies of 30, 16, and 5kV. The final lamella was used for investigation in TEM.

**TEM and STEM Imaging/Spectroscopy:** TEM imaging, selected area electron diffraction (SAED) as well as STEM imaging and spectroscopy were performed on a FEI Osiris operated at 200kV and equipped with a Super-X energy dispersive X-ray spectroscopy (EDS) detector. TEM bright-field images and SAED diffraction patterns have been recorded with a Gatan US1000, STEM BF and high-angle annular dark-field imaging was performed at a semi-convergence angle of  $10.7\text{mrad}$  and a camera length of  $115\text{mm}$ , corresponding to an acceptance angle of  $55\text{200mrad}$  for HAADF. EDS data was evaluated with Bruker Esprit 2.3.

**AFM Imaging:** AFM data were collected by a Bruker Dimension Icon Atomic Force Microscope. AFM measurements were executed in the tapping mode in air conditions using a silicon cantilever (HQ:NSC15/AL BS, MikroMasch) for morphological characterization of  $\text{WO}_3-x$  film, with an amplitude setpoint of  $228.92\text{mV}$ , and scan rate of  $0.8\text{Hz}$ .

**XRD:** XRD was performed on printed  $\text{WO}_3-x$  films at room temperature using a STOE Stadi P diffractometer equipped with a Ga-jet X-ray source (Ga-K $\beta$  radiation,  $1.2079\text{\AA}$ ).

**Electrical Measurement:** All electrical characterizations were carried out at room temperature with a semiconductor parameter analyzer (4200A-SCS, Keithley). The device under test was probed with a probe station (MPS 150, Cascade) connected to the semiconductor parameter analyzer. For all electrical characterization, the Ag top electrode was electrically stimulated while the Au bottom electrode remains grounded all the time.

For post-synaptic current measurement, the voltage waveform was generated by a Keithley 4225-PMU and 4225-RPM. The post-synaptic current was indirectly obtained with an oscilloscope (DL6104, Yokogawa) with a passive 10:1 attenuated probe (701939, Yokogawa) by measuring the voltage over a load resistor  $R_L = 1.43\text{M}\Omega$ , which was attached in series to the memristor. To reduce the impact of measurement noise, a passive digital low-pass filter with a cutoff-frequency of  $f_c = 8\text{kHz}$  was used.

## Supporting Information

Supporting Information is available from the Wiley Online Library or from the author.

## Acknowledgements

This work was funded by the Deutsche Forschungsgemeinschaft (DFG, German Research Foundation) under Germany's Excellent Strategy-2082/1-390761711(Cluster of Excellence "3D Matter Made to Order", 3DMM2O). H.H. acknowledges financial support from the Carl Zeiss Foundation. G.C.M., Y.L., and J.A.-H. acknowledge financial support from the German's Excellent Strategy (Excellent Cluster "3D Matter Made to Order"). A.S. acknowledges financial support from the BMBF project SensIC. The authors thank Karlsruhe Nano Micro Facility (KNMF), a Helmholtz Research Infrastructure at Karlsruhe Institute of Technology (KIT) for support and access to FIB facilities.

Open access funding enabled and organized by Projekt DEAL.

## Conflict of Interest

The authors declare no conflict of interest.

## Data Availability Statement

The data that support the findings of this study are available from the corresponding author upon reasonable request.

## Keywords

inkjet printing, memristors, metal oxides, neuromorphic computing, non-volatile memory

Received: February 27, 2023

Revised: June 2, 2023

Published online:

- [1] D. F. Fernandes, C. Majidi, M. Tavakoli, *J. Mater. Chem. C* **2019**, *7*, 14035.
- [2] J. Machiels, A. Verma, R. Appeltans, M. Buntinx, E. Ferraris, W. Deferme, *Procedia CIRP* **2021**, *96*, 115.
- [3] W. J. Scheideler, V. Subramanian, *Appl. Phys. Lett.* **2022**, *121*, 220502.
- [4] D. D. Weller, M. Hefenbrock, M. Beigl, J. Aghassi-Hagmann, M. B. Tahoori, *Sci. Rep.* **2021**, *11*, 1.
- [5] M. Wang, J. Tu, Z. Huang, T. Wang, Z. Liu, F. Zhang, W. Li, K. He, L. Pan, X. Zhang, X. Feng, Q. Liu, M. Liu, X. Chen, *Adv. Mater.* **2022**, *34*, 2201962.
- [6] M. Lanza, A. Sebastian, W. D. Lu, M. Le Gallo, M.-F. Chang, D. Akinwande, F. M. Puglisi, H. N. Alshareef, M. Liu, J. B. Roldan, *Science* **2022**, *376*, eabj9979.
- [7] E. Covi, E. Donati, X. Liang, D. Kappel, H. Heidari, M. Payvand, W. Wang, *Front. Neurosci.* **2021**, *4*, 2200076.
- [8] C. D. Schuman, S. R. Kulkarni, M. Parsa, J. P. Mitchell, B. Kay, P. Date, *Nat. Comput. Sci.* **2022**, *2*, 10.
- [9] S. Hamdioui, L. Xie, H. A. Du Nguyen, M. Taouil, K. Bertels, H. Corporaal, H. Jiao, F. Catthoor, D. Wouters, L. Eike, J. van Lunteren, in *2015 Design, Automation & Test in Europe Conference & Exhibition (DATE)*. IEEE, Piscataway, NJ, **2015**, pp. 1718–1725.
- [10] G. W. Burr, R. M. Shelby, A. Sebastian, S. Kim, S. Kim, S. Sidler, K. Virwani, M. Ishii, P. Narayanan, A. Fumarola, L. L. Sanches, I. Boybat, M. L. Gallo, K. Moon, J. Woo, H. Hwang, Y. Leblebici, *Adv. Phys.: X* **2017**, *2*, 89.
- [11] A. Sebastian, M. Le Gallo, R. Khaddam-Aljameh, E. Eleftheriou, *Nat. Nanotechnol.* **2020**, *15*, 529.
- [12] H. Amrouch, N. Du, A. Gebregiorgis, S. Hamdioui, I. Polian, in *2021 IFIP/IEEE 29th Int. Conf. on Very Large Scale Integration (VLSI-Soc)*. IEEE, Piscataway, NJ, **2021**, pp. 1–6.
- [13] D. S. Jeong, I. Kim, M. Ziegler, H. Kohlstedt, *RSC Adv.* **2013**, *3*, 3169.
- [14] Y. van De Burgt, A. Melianas, S. T. Keene, G. Malliaras, A. Salleo, *Nat. Electron.* **2018**, *1*, 386.
- [15] V. K. Sangwan, M. C. Hersam, *Nat. Nanotechnol.* **2020**, *15*, 517.
- [16] P. Yao, H. Wu, B. Gao, S. B. Eryilmaz, X. Huang, W. Zhang, Q. Zhang, N. Deng, L. Shi, H.-S. P. Wong, H. Qian, *Nat. Commun.* **2017**, *8*, 1.
- [17] X. Li, J. Tang, Q. Zhang, B. Gao, J. J. Yang, S. Song, W. Wu, W. Zhang, P. Yao, N. Deng, L. Deng, Y. Xie, H. Qian, H. Wu, *Nat. Nanotechnol.* **2020**, *15*, 776.
- [18] E. Linn, R. Rosezin, C. Kügeler, R. Waser, *Nat. Mater.* **2010**, *9*, 403.
- [19] N. Casa Branca, J. Deuermeier, J. Martins, E. Carlos, M. Pereira, R. Martins, E. Fortunato, A. Kiazadeh, *Adv. Electron. Mater.* **2020**, *6*, 1900958.
- [20] M. Delfag, G. Rachovitis, Y. González, J. Jehn, A. H. Youssef, C. Schindler, A. Ruediger, *Flexible Printed Electron.* **2022**, *7*, 045001.
- [21] M. Delfag, R. Katoch, J. Jehn, Y. Gonzalez, C. Schindler, A. Ruediger, *Flexible Printed Electron.* **2021**, *6*, 035011.

- [22] L. Yang, H. Hu, A. Scholz, F. Feist, G. Cadilha Marques, S. Kraus, N. M. Bojanowski, E. Blasco, C. Barner-Kowollik, J. Aghassi-Hagmann, M. Wegener, *Nat. Commun.* **2023**, *14*, 1103.
- [23] H. Hu, A. Scholz, S. A. Singaraju, Y. Tang, G. C. Marques, J. Aghassi-Hagmann, *Appl. Phys. Lett.* **2021**, *119*, 112103.
- [24] E. Carlos, J. Deuermeier, R. Branquinho, C. Gaspar, R. Martins, A. Kiazadeh, E. Fortunato, *J. Mater. Chem. C* **2021**, *9*, 3911.
- [25] G. Vescio, A. Crespo-Yepes, D. Alonso, S. Claramunt, M. Porti, R. Rodriguez, A. Cornet, A. Cirera, M. Nafria, X. Aymerich, *IEEE Electron Device Lett.* **2017**, *38*, 457.
- [26] B. Qu, H. Du, T. Wan, X. Lin, A. Younis, D. Chu, *Mater. Des.* **2017**, *129*, 173.
- [27] X. Feng, Y. Li, L. Wang, S. Chen, Z. G. Yu, W. C. Tan, N. Macadam, G. Hu, L. Huang, L. Chen, X. Gong, D. Chi, T. Hasan, A. V.-Y. Thean, Y.-W. Zhang, K.-W. Ang, *Adv. Electron. Mater.* **2019**, *5*, 1900740.
- [28] B. Salonikidou, T. Yasunori, B. Le Borgne, J. England, T. Shizuo, R. A. Sporea, *ACS Appl. Electron. Mater.* **2019**, *1*, 2692.
- [29] B. Salonikidou, A. Mehonic, Y. Takeda, S. Tokito, J. England, R. A. Sporea, *Adv. Eng. Mater.* **2022**, *24*, 2200439.
- [30] K. Yan, J. Li, L. Pan, Y. Shi, *APL Mater.* **2020**, *8*, 120705.
- [31] K.-S. Kwon, M. K. Rahman, T. H. Phung, S. D. Hoath, S. Jeong, J. S. Kim, *Flexible Printed Electron.* **2020**, *5*, 043003.
- [32] C. Du, F. Cai, M. A. Zidan, W. Ma, S. H. Lee, W. D. Lu, *Nat. Commun.* **2017**, *8*, 2204.
- [33] Y. Zhong, J. Tang, X. Li, X. Liang, Z. Liu, Y. Li, Y. Xi, P. Yao, Z. Hao, B. Gao, H. Qian, H. Wu, *Nat. Electron.* **2022**, *5*, 672.
- [34] C. Li, X. Zhang, P. Chen, K. Zhou, J. Yu, G. Wu, D. Xiang, H. Jiang, M. Wang, Q. Liu, *Iscience* **2023**, 106315.
- [35] M. Klinger, A. Jäger, *J. Appl. Crystallogr.* **2015**, *48*, 2012.
- [36] Y. Seto, M. Ohtsuka, *J. Appl. Crystallogr.* **2022**, *55*, 2.
- [37] G. Roberts, F. W. Schmidlin, *Phys. Rev.* **1969**, *180*, 785.
- [38] J. Zhu, T. Zhang, Y. Yang, R. Huang, *Appl. Phys. Rev.* **2020**, *7*, 011312.
- [39] M. Lanza, R. Waser, D. Ielmini, J. J. Yang, L. Goux, J. Suñe, A. J. Kenyon, A. Mehonic, S. Spiga, V. Rana, S. Wiefels, S. Menzel, I. Valov, M. A. Villena, E. Miranda, X. Jing, F. Campabadal, M. B. Gonzalez, F. Aguirre, F. Palumbo, K. Zhu, J. B. Roldan, F. M. Puglisi, L. Larcher, T.-H. Hou, T. Prodromakis, Y. Yang, P. Huang, T. Wan, Y. Chai, et al., *ACS Nano* **2021**, *15*, 17214.
- [40] S. Wiefels, M. Von Witzleben, M. Hüttemann, U. Böttger, R. Waser, S. Menzel, *IEEE Trans. Electron Devices* **2021**, *68*, 1024.
- [41] M. A. Lastras-Montano, K.-T. Cheng, *Nat. Electron.* **2018**, *1*, 466.
- [42] Z. Wang, H. Wu, G. W. Burr, C. S. Hwang, K. L. Wang, Q. Xia, J. J. Yang, *Nat. Rev. Mater.* **2020**, *5*, 173.
- [43] J. J. Yang, M. D. Pickett, X. Li, D. A. Ohlberg, D. R. Stewart, R. S. Williams, *Nat. Nanotechnol.* **2008**, *3*, 429.
- [44] J. J. Yang, J. Borghetti, D. Murphy, D. R. Stewart, R. S. Williams, *Adv. Mater.* **2009**, *21*, 3754.
- [45] T. Chang, S.-H. Jo, K.-H. Kim, P. Sheridan, S. Gaba, W. Lu, *Appl. Phys. A* **2011**, *102*, 857.
- [46] R. Yang, K. Terabe, T. Tsuruoka, T. Hasegawa, M. Aono, *Appl. Phys. Lett.* **2012**, *100*, 231603.
- [47] R. Dittmann, S. Menzel, R. Waser, *Adv. Phys.* **2021**, *70*, 155.
- [48] A. Citri, R. C. Malenka, *Neuropsychopharmacology* **2008**, *33*, 18.
- [49] P. P. Atluri, W. G. Regehr, *J. Neurosci.* **1996**, *16*, 5661.
- [50] R. S. Zucker, W. G. Regehr, *Annu. Rev. Physiol.* **2002**, *64*, 355.
- [51] R. S. Zucker, *Annu. Rev. Neurosci.* **1989**, *12*, 13.
- [52] D. V. Buonomano, M. M. Merzenich, *Science* **1995**, *267*, 1028.
- [53] Y. Lin, F. Meng, T. Zeng, Q. Zhang, Z. Wang, Y. Cheng, X. Zhao, L. Gu, H. Xu, Y. Liu, *Adv. Funct. Mater.* **2023**, 2302787.
- [54] D. Li, B. Wu, X. Zhu, J. Wang, B. Ryu, W. D. Lu, W. Lu, X. Liang, *ACS Nano* **2018**, *12*, 9240.
- [55] H. Kamiya, R. S. Zucker, *Nature* **1994**, *371*, 603.
- [56] R. S. Zucker, *J. Physiol.* **1974**, *241*, 91.
- [57] S. A. Fisher, T. M. Fischer, T. J. Carew, *Trends Neurosci.* **1997**, *20*, 170.
- [58] K. Magleby, J. Zengel, *J. Physiol.* **1976**, *257*, 449.
- [59] S. Hu, Y. Liu, T. Chen, Z. Liu, Q. Yu, L. Deng, Y. Yin, S. Hosaka, *Appl. Phys. Lett.* **2013**, *103*, 133701.
- [60] V. Pena, A. Rivera, C. Leon, J. Santamaria, E. Garcia-Gonzalez, J. Gonzalez-Calbet, *Chem. Mater.* **2002**, *14*, 1606.
- [61] D. Magleby, J. E. Zengel, *J. Physiol.* **1976**, *260*, 687.
- [62] S. A. Josselyn, S. Tonegawa, *Science* **2020**, *367*, eaaw4325.
- [63] R. Lamprecht, J. LeDoux, *Nat. Rev. Neurosci.* **2004**, *5*, 45.
- [64] W. C. Abraham, *Nat. Rev. Neurosci.* **2008**, *9*, 387.
- [65] A. Laborieux, M. Ernoult, T. Hirtzlin, D. Querlioz, *Nat. Commun.* **2021**, *12*, 1.
- [66] F. T. Zohora, A. M. Zyarah, N. Soares, D. Kudithipudi, in *2020 IEEE Int. Sympos. on Circuits and Syst. (ISCAS)*. IEEE, Piscataway, NJ, **2020**, pp. 1–5.
- [67] D. Andina, A. Alvarez-Vellisco, J. Aleksandar, J. Fombellida, *Intell. Autom. Soft Comput.* **2009**, *15*, 683.
- [68] L. Abbott, W. G. Regehr, *Nature* **2004**, *431*, 796.
- [69] V. Parmar, S. K. Kingra, M. Suri, *J. Phys. D: Appl. Phys.* **2018**, *51*, 454004.
- [70] E. S. Fortune, G. J. Rose, *Trends Neurosci.* **2001**, *24*, 381.